# Semi-Dirac and Weyl Fermions in Transition Metal Oxides*

Narayan Mohanta,[1] Jong Mok Ok,[1] Jie Zhang,[1] Hu Miao,[1] Elbio Dagotto,[1,2] Ho Nyung Lee,[1] and Satoshi Okamoto[1]

[1] *Materials Science and Technology Division, Oak Ridge National Laboratory, Oak Ridge, TN 37831, USA*
[2] *Department of Physics and Astronomy, The University of Tennessee, Knoxville, TN 37996, USA*

We show that a class of compounds with $I4/mcm$ crystalline symmetry hosts three-dimensional semi-Dirac fermions. Unlike the known two-dimensional semi-Dirac points, the degeneracy of these three-dimensional semi-Dirac points is not lifted by spin-orbit coupling due to the protection by a nonsymmorphic symmetry — screw rotation in the $a$-$b$ plane and a translation along the $c$ axis. This crystalline symmetry is found in tetragonal perovskite oxides, realizable in thin films by epitaxial strain that results in $a^0a^0c^-$-type octahedral rotation. Interestingly, with broken time-reversal symmetry, two pairs of Weyl points emerge from the semi-Dirac points within the Brillouin zone, and an additional lattice distortion leads to enhanced intrinsic anomalous Hall effect. We discuss possible fingerprints of this symmetry-protected band topology in electronic transport experiments.



Protected band degeneracy continues being a fundamental topic of interest to understand the physics of various topological semimetals, *e.g.* Dirac, Weyl, and nodal loop semimetals [1–6]. The guiding principle to classify these topological semimetals has been the presence of one or more symmetries that allow degenerate eigenstates [7, 8]. Spin-orbit coupling (SOC) lifts the band degeneracies everywhere except at momenta where symmetry enforces that the matrix elements of the SOC operator vanish [9]. Since SOC is present in all materials, the implication is that unless there is a special symmetry that protects the band degeneracy, the topological nodal semimetals exist in the theoretically-idealized case when SOC is zero.

Semi-Dirac fermions in two-dimensional solids connect the physics of monolayer graphene that exhibits linear band dispersion near the Dirac points and bilayer graphene that has quadratic band dispersion near the band-touching points [10, 11]. The semi-Dirac points, in which both linear and quadratic band dispersions occur along different momentum directions, exist in the absence of SOC, in various systems including hexagonal lattices under a magnetic field [12], $VO_2$-$TiO_2$ heterostructures [13, 14], BEDT-$TTF_2I_3$ salt under pressure [15], silicene oxide [16], photonic crystals [17], and Hofstadter spectrum [18]. The quadratic dispersion along one of the momentum directions leads to an enhanced density of states at low energies as compared to linear Dirac dispersion, making instabilities relatively easier to occur due to the enlarged phase space for quantum fluctuations [19]. A semi-Dirac semimetal becomes a Chern insulator, revealing quantized anomalous Hall conductivity with broken time-reversal symmetry (TRS), in the presence of SOC that opens an energy gap at the semi-Dirac point [20]. A similar Chern insulating state is also induced in a semi-Dirac semimetal with two gapless Dirac nodes by impinging a circularly polarized light [21]. In multilayer $(TiO_2)_m/(VO_2)_n$ heterostructures, the semi-Dirac point is not destroyed by SOC in a special situation when the spins are aligned along the rutile $c$ axis [22].

However, the questions that remain open are whether there exists a natural material in which the semi-Dirac point is gapless generically when SOC is present and whether these semi-Dirac points exist in a higher dimension. Here, we show that a class of materials hosts three-dimensional (3D) gapless semi-Dirac fermions in the presence of SOC. Tetragonal perovskite oxides with $I4/mcm$ crystalline symmetry (space group 140) exhibit such 3D semi-Dirac points at a high-symmetry point, and its nonsymmorphic symmetry protects the semi-Dirac points against the gap-opening by SOC. Nonsymmorphic symmetry-protected two-dimensional Dirac semimetallic phase was proposed in a theoretical model [23], and subsequent studies using *ab initio* calculations in layered compounds [24, 25]. Cubic perovskite oxide thin films can be transformed into the tetragonal phase to realize the $I4/mcm$ space group under epitaxial strain that produces $a^0a^0c^-$-type (in the Glazer notation) octahedral rotation [26, 27]. The out-of-phase octahedral rotation brings in the nonsymmorphic symmetry: screw rotation $2\pi/\theta$ ($\theta$ is the rotation angle), translation along [001] $z \to z+1/2$, as shown in Fig. 1(a). A consequence of the fractional translational symmetry is that the unit cell of the original symmorphic crystal is doubled. In this case, the folded back bands stick together necessarily at the Brillouin-zone boundary if the nonsymmorphic symmetry is present, even with SOC.

As a particular physical realization of the $I4/mcm$ space group, we primarily focus on tetragonal $SrNbO_3$ that manifestly displays the defining characteristics of this nonsymmorphic symmetry, and a 3D semi-Dirac point appears close to the Fermi energy at a high-symmetry point P at the Brillouin-zone boundary. Three

* This manuscript has been authored by UTBattelle, LLC under Contract No. DE-AC05-00OR22725 with the U.S. Department of Energy. The United States Government retains and the publisher, by accepting the article for publication, acknowledges that the United States Government retains a non-exclusive, paid-up, irrevocable, world-wide license to publish or reproduce the published form of this manuscript, or allow others to do so, for United States Government purposes. The Department of Energy will provide public access to these results of federally sponsored research in accordance with the DOE Public Access Plan (http://energy.gov/downloads/doepublic-access-plan)

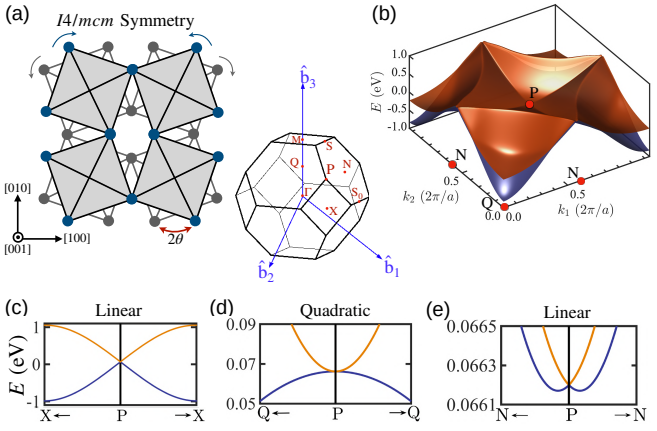


FIG. 1. (a) Illustration of the octahedral rotation-driven tetragonal phase of perovskite oxides. $a^0a^0c^-$-type rotation in a cubic crystal produces $I4/mcm$ space group that exhibits the nonsymmorphic symmetry (screw rotation in the $a$-$b$ plane and translation along the $c$ axis). (b) Dispersion of two electronic bands in the P-Q-N plane. (c)-(e) show the dispersion curves along different momentum paths. The inset in the middle shows the high-symmetry points in the Brillouin zone.

different kinds of dispersion emerge from this semi-Dirac point—linear along the P-X direction, quadratic along the P-Q direction, and linear in the close vicinity of the P point along along the P-N direction, as shown in Fig. 1(b)-(e). With a TRS-breaking element such as an external magnetic field, we show that two pairs of Weyl points appear within the Brillouin zone. The opposite zone boundaries share one pair of Weyl points. The presence of Weyl points in a semi-Dirac semimetal leads to unique properties such as highly-anisotropic plasmon frequency, unusual carrier density-dependence of the Hall coefficient, and the divergence of the ratio of orbital to spin susceptibilities at low carrier doping [28]. The Weyl points in tetragonal $SrNbO_3$ open up an energy gap in the presence of an additional broken inversion symmetry, obtained by a small displacement at a Nb site. We show that this gapped Weyl points, at the P point, exhibits an enhanced intrinsic anomalous Hall effect. With these intriguing properties, perovskite oxides of the $I4/mcm$ space group provide a unique example of a class of compounds that hosts crystalline symmetry-protected 3D semi-Dirac fermions. Our Berry curvature analysis sheds light on the unusual features in transport experiments, such as the Shubnikov de Haas oscillations and anomalous Hall effect measurements. Furthermore, the ability to control the Berry phase by octahedral rotation shows a pathway towards developing devices for oxide-based electronics.

*Electronic structure:* The band dispersion of tetragonal $SrNbO_3$ in the presence of SOC, obtained from our *ab initio* calculations [29] along various high-symmetry momenta in the Brillouin zone is shown in Figs. 2(a). The three $t_{2g}$ orbitals of Nb $4d$ state predominantly populate the Fermi level, as in the case of cubic $SrNbO_3$ [30, 31]. Due to the zone folding at the Brillouin zone boundary, the bands along the P-N momentum direction are four-fold degenerate in the absence of SOC, creating line nodes. The degeneracy of these nodal lines is lifted everywhere, except at the high symmetry points, when SOC is turned on, as described in 2(b). The TRS and the nonsymmorphic symmetry protect the four-fold degeneracy at the P point, giving rise to the 3D semi-Dirac point at an energy approximately 0.0662 eV above the Fermi level. Three other Dirac points appear at the N point at energies 0.5 eV above the Fermi level. Being away from the Fermi level, the Dirac points at the N point may not be accessible to electronic transport; here we, therefore, focus on the semi-Dirac point at the P point. Yet, replacing Nb with other transition-metal element such as Mo might tune the Fermi level close to the Dirac points at the N point. The Fermi surfaces of the three spin-orbit coupled $t_{2g}$ orbitals are depicted in Fig. 2(c)-(e). Due to the linear dispersion near the semi-Dirac point, a small doping by external gating or chemical doping can tune the Fermi level to the semi-Dirac point, creating the possibility to obtain a quantized Berry phase and a very high-mobility conduction [32–34]. Also, the presence of the semi-Dirac points in the asymmetric, convex Fermi surface is expected to produce a large nonsaturating magnetoresistance [35–37].

*Topological invariant:* We investigate the topological properties of the compound under consideration, tetragonal $SrNbO_3$, by using two protocols—first, by looking at the Berry curvature, and second, by computing the topological invariant of the Bloch bands. The Berry cur-

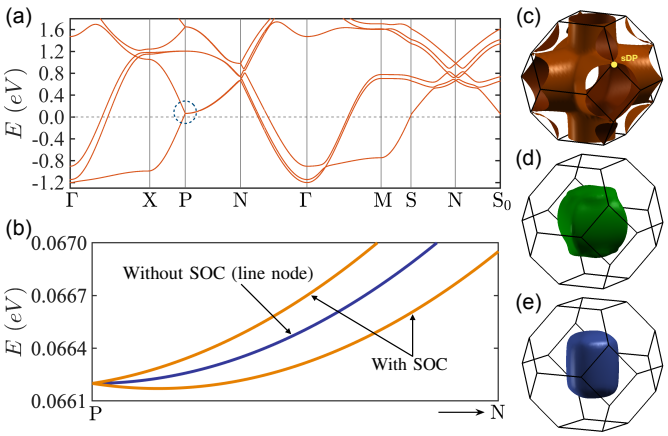


FIG. 2. (a) Band dispersion of tetragonal $SrNbO_3$ in the presence of spin-orbit coupling, through various high-symmetry momenta in the Brillouin zone. (b) Expanded view of the dispersion along the P-N direction, without and with spin-orbit coupling. (c)-(e) The three Fermi surfaces of the spin-orbit coupled $t_{2g}$ bands at the Fermi level. The semi-Dirac point (sDP) is denoted by the dashed circle at the P point in (a) and by the yellow dot in (c).

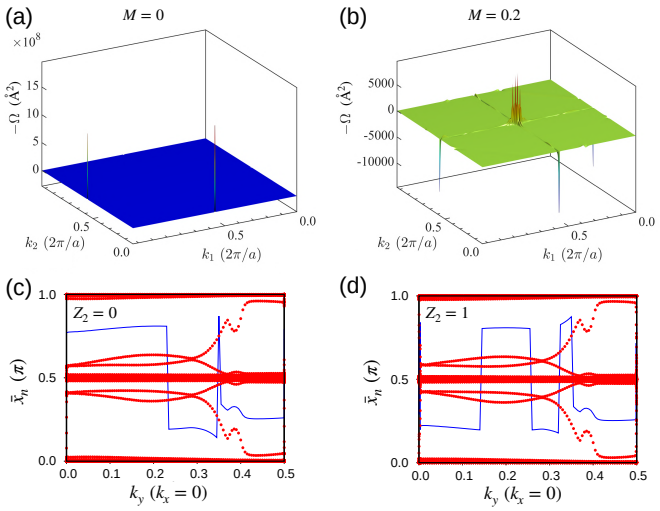


FIG. 3. Berry curvature $\Omega(\mathbf{k})$ for Nb spin polarization (a) $M=0$, and (b) $M=0.2$, plotted in a momentum plane containing the P point at the center, and the N points at the side centers. We use a dense $100\times100$ momentum grid. (c), (d) The Wannier charge centers $\bar{x}_n$ along momentum $k_y$ with $k_x=0$ for (a) $M=0$, and (b) $M=0.2$. The blue line represents the center of the maximum gap between the Wannier charge centers. In (d), the gap center crosses the Wannier charge centers an odd number of times, resulting in a topological index $Z_2=1$.

vature is given by [38]

$$\Omega(\mathbf{k}) = -\sum_{m,n}^{\varepsilon_{m\mathbf{k}}\neq\varepsilon_{n\mathbf{k}}} 2\,\mathrm{Im}\frac{\langle\psi_{n\mathbf{k}}|v_x|\psi_{m\mathbf{k}}\rangle\langle\psi_{m\mathbf{k}}|v_y|\psi_{n\mathbf{k}}\rangle}{(\varepsilon_{m\mathbf{k}}-\varepsilon_{n\mathbf{k}})^2}, \quad (1)$$

where $|\psi_{n\mathbf{k}}\rangle$ is the spinor Bloch wave function of the $n^{\text{th}}$ band with eigenenergy $\varepsilon_{n\mathbf{k}}$, and $\mathbf{v}=(v_x,v_y)$ is the velocity operator. We use Wannier interpolation based on maximally-localized Wannier functions [39, 40]. The Berry curvature in the P$-$N$-$Q plane, the same plane considered in Fig. 1(b), is shown in Fig. 3(a). The semi-Dirac point, being gapless, reveals zero Berry curvature at the center P point. We introduce TRS breaking and opening of an energy gap at the semi-Dirac point by constraining to a spin polarization at the Nb sites. Fig. 3(b) shows a large Berry curvature contributions at and near the P point with $M=0.2$, which represents 20% spin polarization along the $+z$ direction. $M$ is defined as $M=\sum_{a\in\text{Nb }t_{2g}\text{ orbitals}}\langle n_{a,\uparrow}\rangle-\langle n_{a,\downarrow}\rangle$, where $n_{a,\uparrow}$ is the occupation of electrons at orbital $a$ and spin $\uparrow$. The enhanced Berry curvature induced by a nonzero $M$ strongly suggests the nontrivial band topology. To check this possibility, we compute the topological invariant via the Wannier charge centers $\bar{x}_n$, corresponding to the Wannier functions that are maximally localized in one dimension, defined as [41]

$$\bar{x}_n = \frac{i}{2\pi}\int_{-\pi}^{\pi} d\mathbf{k}\langle u_{n\mathbf{k}}|\partial_{\mathbf{k}}|u_{n\mathbf{k}}\rangle, \quad (2)$$

where $|u_{n\mathbf{k}}\rangle = e^{-i\mathbf{k}\cdot\mathbf{r}}|\psi_{n\mathbf{k}}\rangle$ represents the periodic parts of the Block states. In Fig. 3(c) and 3(d), we show the evolution of the Wannier charge centers with the momentum $k_y$ for, respectively, $M=0$, and $M=0.2$. With $M=0.2$, the center of the largest gap between the Wannier charge centers (blue line) crosses the Wannier charge centers odd number of times in traversing a path from $k_y=0$ to $k_y=\pi/a$, yielding a topological invariant $Z_2=1$. A non-zero $Z_2$ index in a Chern insulator with broken TRS usually predicts a quantum anomalous Hall effect. We, however, find that the Hall conductivity is not quantized, and the semi-Dirac points in tetragonal $SrNbO_3$ may, therefore, be classified as type I [20], similar to that proposed in $VO_2$-$TiO_2$ heterostructures [14]. This is also verified by the absence of a band crossing of the surface states [29].

*Anomalous Hall effect:* In the absence of TRS, *e.g.* with an external magnetic field that is applied perpendicular to the $a$-$b$ plane, the semi-Dirac point in the $I4/mcm$ space group compounds splits into two Weyl nodes, as illustrated in Fig. 4(a). In the considered tetragonal $SrNbO_3$, we find that a finite magnetization at the Nb sites generates a Weyl point close to the P point, as shown in Fig. 4(b). The pair of Weyl points appears along the P-X-P momentum direction, totaling two pairs in the entire Brillouin zone, as shown in the inset of Fig. 4(d). By

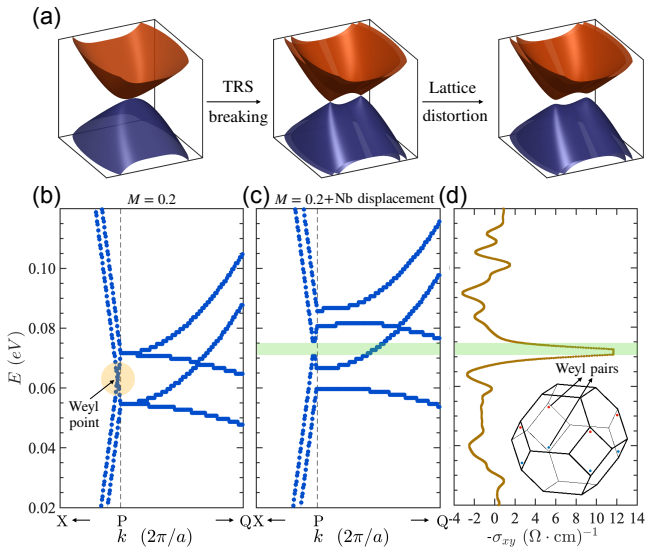


FIG. 4. (a) Illustration of the effect of broken symmetries on the semi-Dirac points. TRS breaking splits the semi-Dirac point into a pair of Weyl points, and additional lattice distortion opens up an energy gap. (b) Band dispersion along the momentum path X-P-Q in the vicinity of the P point, in the presence of the broken time-reversal symmetry that lifts the four-fold degeneracy of the semi-Dirac point at the P point, and creates a pair of Weyl points near the P point. (c) The Weyl point acquires an energy gap in the presence of an inversion symmetry-breaking lattice distortion. (d) The anomalous Hall conductivity, with varying energy, reveals a plateau within the energy gap at the Weyl point. Inset in (d) shows the two pairs of the Weyl points within the Brillouin zone, appearing near the P point.

lowering the lattice symmetry further, an energy gap is induced at the Weyl points. We consider a lattice distortion that lowers the inversion symmetry but preserves the nonsymmorphic symmetry. This is achieved by shifting the center Nb site vertically by a small amount. Such a distortion may be realized naturally by epitaxial strain induced by lattice mismatch with the substrate at a polar interface, or by applying an electric field perpendicular to the interface. Fig. 4(c) shows a distortion-induced energy gap at a Weyl point. In a truly semimetallic system, such an energy gap gives rise to quantum anomalous Hall effect in the vicinity of the Dirac or semi-Dirac point. In tetragonal $SrNbO_3$, a net quantization is not achieved due to the presence of other bands at the Fermi level and instead an enhanced intrinsic anomalous Hall effect is expected to appear within the energy gap, as shown in Fig. 4(d). We find that the anomalous Hall conductivity is dependent on the amount of distortion in the tetragonal lattice, and the octahedral rotation, suggesting another route to obtain tunable anomalous Hall effect in oxide interfaces.

*Tunable Berry phase:* Understanding the Berry phase-driven phenomena in perovskite oxides is fundamentally important, not only to realize emergent electromagnetism in a feasible way, but also to identify the origin of non-trivial Hall signatures. In oxide compounds where magnetism coexists with a non-trivial band topology, such as $SrRuO_3$, the intrinsic anomalous Hall effect appears without any external magnetic field [42]. In the non-magnetic tetragonal perovskites, like the one considered here *i.e.* $SrNbO_3$, doping magnetic impurities or applying an external magnetic field leads to a finite Berry phase in the Bloch bands. We find that the Berry curvature $\Omega$ can be tuned externally by changing the octahedral rotation angle $\theta$ [29]. Particularly, the Berry curvature and the resulting anomalous Hall conductivity vary non-monotonically with increasing $\theta$. Previous experiments have demonstrated that external strain modulation can control octahedral rotations in oxide thin films [43, 44]. Our presented results, therefore, show an effective way to control the Berry phase and consequently the topological properties of perovskite transition-metal oxides by epitaxial strain engineering.

*Effective low-energy model:* To study the low-energy behavior of the 3D semi-Dirac dispersion, we derive an effective tight-binding model for the SOC-coupled $t_{2g}$ electrons in tetragonal perovskite oxides [29]. From this tight-binding Hamiltonian, we obtain the following low-energy Hamiltonian that describes the 3D semi-Dirac dispersion around the P point

$$H_{\text{low–E}} = -A\big(k_x^2+k_y^2\big)\tau_0\sigma_0 - B(-k_x\tau_3\sigma_1 - k_y\tau_3\sigma_2) - \Big\{C\big(k_x^2-k_y^2\big) - Dk_z\Big\}\tau_1\sigma_0, \quad (3)$$

where $\sigma_i$ and $\tau_i$ are the Pauli matrices in the spin space and the sublattice space; $A$, $B$, $C$, and $D$ are parameters. The partial density of states surrounding the semi-Dirac point, exhibits a depletion at the energy at which the semi-Dirac point appears [29], rather than a minimum as in the isotropic Dirac or 2D semi-Dirac cases [45]. A depletion of the density of states near the Fermi energy usually indicates a strong effect of electronic correlation or disorder [46]. The mutual interplay of these additional effects in the present semi-Dirac compound may, therefore, produce unconventional properties.

*Discussion:* We further analyzed the electronic properties of four other compounds from the $I4/mcm$ space group, *viz.* $CaNbO_3$, $SrRuO_3$, $SrMoO_3$, and $SrTiO_3$ and confirmed the presence of the 3D semi-Dirac fermions at the P point [29]. This establishes that the discussed symmetry-protected band topology is generic to tetragonal perovskite oxides that belong to this space group, the only difference being the location in energy of the semi-Dirac points. For $CaNbO_3$ and $SrRuO_3$, the semi-Dirac point at the P point is closer to the Fermi level than in $SrNbO_3$. On the other hand, $SrTiO_3$, having a large energy gap at the Fermi level, the semi-Dirac points are situated far away from the Fermi level. Using $SrTiO_3$ as a substrate is, therefore, beneficial for providing epitaxial strain. For $SrMoO_3$ and $SrRuO_3$, three Dirac points at the N point are also located close to the Fermi level which indicates that these two compounds can be interesting also to explore the influence of the non-trivial band topology in transport experiments.

In contrast to the isotropic Dirac semimetals, the semi-Dirac semimetals can be realized at a quantum critical point between a 3D Dirac semimetal and a topologically trivial insulator [47, 48]. In response to a circularly polarized light, the semi-Dirac semimetals with a gapless Dirac node do not open an energy gap, unlike the isotropic Dirac semimetals [49]. Tetragonal perovskite oxides, therefore, offer a feasible material platform to study new phenomena that cannot be found in known Dirac semimetals.

The interplay of Coulomb interaction and disorder in a two-dimensional semi-Dirac semimetal gives rise to a variety of quantum phase transitions and non-Fermi liquid behaviors [50]. Disorder, particularly, has a profound effect as it can drive a Lifshitz transition from an insulator to a semimetal, and a topological transition to a Chern insulating state [51]. The interplay of topology, disorder and Coulomb interaction in the nonsymmorphic symmetry-protected semi-Dirac fermions, found in the tetragonal perovskite oxides, can lead to even richer physical properties due to their three-dimensional nature.

To conclude, we have shown that non-magnetic tetragonal perovskite oxides with $I4/mcm$ symmetry, *e.g.* $SrNbO_3$, $CaNbO_3$, and $SrMoO_3$, host 3D semi-Dirac fermions that are protected by a nonsymmorphic symmetry. This crystalline symmetry can be realized by a substrate strain when the cubic perovskites undergo an octahedral rotation of type $a^0a^0c^-$. Due to the symmetry protection, the semi-Dirac degeneracy is maintained in the presence of SOC, making this class of compounds a unique, natural example. Breaking the TRS leads to two pairs of Weyl points from the semi-Dirac points. In the presence of an additional inversion symmetry-

breaking lattice distortion, the Weyl points acquire an energy gap, and an enhanced intrinsic anomalous Hall effect is realized. The presence of the Weyl points is expected to produce negative magnetoresistance induced by chiral anomaly [52]. The Berry phase arising due to the semi-Dirac point with a broken symmetry is tunable by controlling the octahedral rotation angle that can be changed by the sample thickness, or advanced interface engineering. Our findings serve as an important stepping stone towards understanding various kinds of quasiparticles that can be found in solids [53–55].

*Acknowledgements:* This work was supported by the U.S. Department of Energy, Office of Science, Basic Energy Sciences, Materials Sciences and Engineering Division.

[1] C. Herring, "Accidental degeneracy in the energy bands of crystals," Phys. Rev. **52**, 365 (1937).
[2] A. A. Burkov, M. D. Hook, and Leon Balents, "Topological nodal semimetals," Phys. Rev. B **84**, 235126 (2011).
[3] A. A. Burkov, "Topological semimetals," Nat. Mater. **15**, 1145 (2016).
[4] T. Bzdušek, .
[5] N. P. Armitage, E. J. Mele, and A. Vishwanath, "Weyl and Dirac semimetals in three-dimensional solids," Rev. Mod. Phys. **90**, 015001 (2018).
[6] A.A. Burkov, "Weyl metals," Annu. Rev. Condens. Matter Phys. **9**, 359 (2018).
[7] C.-K. Chiu, J. C. Y. Teo, A. P. Schnyder, and S. Ryu, "Classification of topological quantum matter with symmetries," Rev. Mod. Phys. **88**, 035005 (2016).
[8] S.-Y. Yang, H. Yang, E. Derunova, S. S. P. Parkin, B. Yan, and M. N. Ali, "Symmetry demanded topological nodal-line materials," Adv. Phys.: X **3**, 1414631 (2018).
[9] P. B. Allen and W. E. Pickett, "Accidental degeneracy in k-space, geometrical phase, and the perturbation of $\pi$ by spin-orbit interactions," Physica C: Superconductivity and its Applications **549**, 102 (2018).
[10] A. H. Castro Neto, F. Guinea, N. M. R. Peres, K. S. Novoselov, and A. K. Geim, "The electronic properties of graphene," Rev. Mod. Phys. **81**, 109 (2009).
[11] E. McCann and M. Koshino, "The electronic properties of bilayer graphene," Rep. Prog. Phys. **76**, 056503 (2013).
[12] P. Dietl, F. Piéchon, and G. Montambaux, "New magnetic field dependence of Landau levels in a Graphenelike structure," Phys. Rev. Lett. **100**, 236405 (2008).
[13] V. Pardo and W. E. Pickett, "Half-metallic semi-Dirac-point generated by quantum confinement in $TiO_2/VO_2$ nanostructures," Phys. Rev. Lett. **102**, 166803 (2009).
[14] S. Banerjee, R. R. P. Singh, V. Pardo, and W. E. Pickett, "Tight-binding modeling and low-energy behavior of the semi-Dirac point," Phys. Rev. Lett. **103**, 016402 (2009).
[15] S. Katayama, A. Kobayashi, and Y. Suzumura, "Pressure-induced zero-gap semiconducting state in organic conductor $\alpha$-(BEDT-TTF)$_2$I$_3$ salt," J. Phys. Soc. Jpn **75**, 054705 (2006).
[16] C. Zhong, Y. Chen, Y. Xie, Y.-Y. Sun, and S. Zhang, "Semi-Dirac semimetal in silicene oxide," Phys. Chem. Chem. Phys. **19**, 3820 (2017).
[17] Y. Wu, "A semi-Dirac point and an electromagnetic topological transition in a dielectric photonic crystal," Opt. Express **22**, 1906 (2014).
[18] P. Delplace and G. Montambaux, "Semi-Dirac point in the Hofstadter spectrum," Phys. Rev. B **82**, 035438 (2010).
[19] M. D. Uryszek, E. Christou, A. Jaefari, F. Krüger, and B. Uchoa, "Quantum criticality of semi-Dirac fermions in $2+1$ dimensions," Phys. Rev. B **100**, 155101 (2019).
[20] H. Huang, Z. Liu, H. Zhang, W. Duan, and D. Vanderbilt, "Emergence of a Chern-insulating state from a semi-Dirac dispersion," Phys. Rev. B **92**, 161115 (2015).
[21] K. Saha, "Photoinduced Chern insulating states in semi-Dirac materials," Phys. Rev. B **94**, 081103 (2016).
[22] V. Pardo and W. E. Pickett, "Metal-insulator transition through a semi-Dirac point in oxide nanostructures: $VO_2$ (001) layers confined within $TiO_2$," Phys. Rev. B **81**, 035111 (2010).
[23] S. M. Young and C. L. Kane, "Dirac semimetals in two dimensions," Phys. Rev. Lett. **115**, 126803 (2015).
[24] S. Li, Y. Liu, S.-S. Wang, Z.-M. Yu, S. Guan, X.-L. Sheng, Y. Yao, and S. A. Yang, "Nonsymmorphic-symmetry-protected hourglass Dirac loop, nodal line, and Dirac point in bulk and monolayer $X_3SiTe_6$ (X = Ta, Nb)," Phys. Rev. B **97**, 045131 (2018).
[25] D. Shao, T. Chen, Q. Gu, Z. Guo, P. Lu, J. Sun, L. Sheng, and D. Xing, "Nonsymmorphic symmetry protected node-line semimetal in the trigonal $YH_3$," Sci. Rep. **8**, 1467 (2018).
[26] J. M. Rondinelli and N. A. Spaldin, "Substrate coherency driven octahedral rotations in perovskite oxide films," Phys. Rev. B **82**, 113402 (2010).
[27] J. M. Ok, N. Mohanta, J. Zhang, S. Yoon, S. Okamoto, E. S. Choi, H. Zhou, M. Briggeman, P. Irvin, A. R. Lupini, Y.-Y. Pai, E. Skoropata, C. Sohn, H. Li, H. Miao, R. G. Moore, Z. Ward, B. J. Lawrie, W. S. Choi, G. Eres, J. Levy, and H. N. Lee, "Correlated oxide Dirac semimetal in the extreme quantum limit," Private communication.
[28] S. Banerjee and W. E. Pickett, "Phenomenology of a semi-Dirac semi-Weyl semimetal," Phys. Rev. B **86**, 075124 (2012).
[29] For details, see the Supplemental Materials.
[30] C. Bigi, P. Orgiani, J. Sławińska, J. Fujii, J. T. Irvine, S. Picozzi, G. Panaccione, I. Vobornik, G. Rossi, D. Payne, and F. Borgatti, "Direct insight into the band structure of $SrNbO_3$," Phys. Rev. Mater. **4**, 025006 (2020).
[31] Y. Park, J. Roth, D. Oka, Y. Hirose, T. Hasegawa, A. Paul, A. Pogrebnyakov, V. Gopalan, T. Birol, and R. Engel-Herbert, "$SrNbO_3$ as a transparent conductor in the visible and ultraviolet spectra," Commun. Phys. **3**, 102 (2020).
[32] K. Wang, D. Graf, H. Lei, S. W. Tozer, and C. Petrovic, "Quantum transport of two-dimensional Dirac fermions in $SrMnBi_2$," Phys. Rev. B **84**, 220401 (2011).

[33] T. Liang, Q. Gibson, M. N. Ali, M. Liu, R. J. Cava, and N. P. Ong, "Ultrahigh mobility and giant magnetoresistance in the Dirac semimetal $Cd_3As_2$," Nat. Mater. **14**, 280 (2015).

[34] M. J. Veit, R. Arras, B. J. Ramshaw, R. Pentcheva, and Y. Suzuki, "Nonzero Berry phase in quantum oscillations from giant Rashba-type spin splitting in $LaTiO_3/SrTiO_3$ heterostructures," Nat. Commun. **9**, 1458 (2018).

[35] P. He, C.-H. Hsu, S. Shi, K. Cai, J. Wang, Q. Wang, G. Eda, H. Lin, V. M. Pereira, and H. Yang, "Nonlinear magnetotransport shaped by Fermi surface topology and convexity," Nat. Commun. **10**, 1290 (2019).

[36] A. Vashist, R. K. Gopal, D. Srivastava, M. Karppinen, and Y. Singh, "Fermi surface topology and large magnetoresistance in the topological semimetal candidate PrBi," Phys. Rev. B **99**, 245131 (2019).

[37] S. Zhang, Q. Wu, Y. Liu, and O. V. Yazyev, "Magnetoresistance from Fermi surface topology," Phys. Rev. B **99**, 035142 (2019).

[38] X. Wang, J. R. Yates, I. Souza, and D. Vanderbilt, "*Ab initio* calculation of the anomalous Hall conductivity by Wannier interpolation," Phys. Rev. B **74**, 195118 (2006).

[39] N. Marzari and D. Vanderbilt, "Maximally localized generalized Wannier functions for composite energy bands," Phys. Rev. B **56**, 12847 (1997).

[40] I. Souza, N. Marzari, and D. Vanderbilt, "Maximally localized Wannier functions for entangled energy bands," Phys. Rev. B **65**, 035109 (2001).

[41] A. A. Soluyanov and D. Vanderbilt, "Computing topological invariants without inversion symmetry," Phys. Rev. B **83**, 235401 (2011).

[42] D. J. Groenendijk, C. Autieri, T. C. van Thiel, W. Brzezicki, J. R. Hortensius, D. Afanasiev, N. Gauquelin, P. Barone, K. H. W. van den Bos, S. van Aert, J. Verbeeck, A. Filippetti, S. Picozzi, M. Cuoco, and A. D. Caviglia, "Berry phase engineering at oxide interfaces," Phys. Rev. Research **2**, 023404 (2020).

[43] A. Herklotz, A. T. Wong, T. Meyer, M. D. Biegalski, H. N. Lee, and T. Z. Ward, "Controlling octahedral rotations in a perovskite via strain doping," Sci. Rep. **6**, 26491 (2016).

[44] A. K. Choquette, C. R. Smith, R. J. Sichel-Tissot, E. J. Moon, M. D. Scafetta, E. Di Gennaro, F. Miletto Granozio, E. Karapetrova, and S. J. May, "Octahedral rotation patterns in strained $EuFeo_3$ and other Pbnm perovskite films: Implications for hybrid improper ferroelectricity," Phys. Rev. B **94**, 024105 (2016).

[45] W. Chen, X. Zhu, X. Zhou, and G. Zhou, "Power law decay of local density of states oscillations near a line defect in a system with semi-Dirac points," Phys. Rev. B **103**, 125429 (2021).

[46] H.-J. Noh, T.-U. Nahm, J.-Y. Kim, W.-G. Park, S.-J. Oh, J.-P. Hong, and C.-O. Kim, "Depletion of the density of states near the fermi energy induced by disorder and electron correlation in alloys," Solid State Commun. **116**, 137 (2000).

[47] B.-J. Yang and N. Nagaosa, "Classification of stable three-dimensional Dirac semimetals with nontrivial topology," Nat. Commun. **5**, 4898 (2014).

[48] S. A. Parameswaran, A. M. Turner, D. P. Arovas, and A. Vishwanath, "Topological order and absence of band insulators at integer filling in non-symmorphic crystals," Nat. Phys. **9**, 299 (2013).

[49] A. Narayan, "Floquet dynamics in two-dimensional semi-Dirac semimetals and three-dimensional Dirac semimetals," Phys. Rev. B **91**, 205445 (2015).

[50] P.-L. Zhao, J.-R. Wang, A.-M. Wang, and G.-Z. Liu, "Interplay of Coulomb interaction and disorder in a two-dimensional semi-Dirac fermion system," Phys. Rev. B **94**, 195114 (2016).

[51] P. V. Sriluckshmy, K. Saha, and R. Moessner, "Interplay between topology and disorder in a two-dimensional semi-Dirac material," Phys. Rev. B **97**, 024204 (2018).

[52] D. T. Son and B. Z. Spivak, "Chiral anomaly and classical negative magnetoresistance of Weyl metals," Phys. Rev. B **88**, 104412 (2013).

[53] B. Bradlyn, J. Cano, Z. Wang, M. G. Vergniory, C. Felser, R. J. Cava, and B. A. Bernevig, "Beyond Dirac and Weyl fermions: Unconventional quasiparticles in conventional crystals," Science **353** (2016).

[54] Z. Wang, A. Alexandradinata, R. J. Cava, and B. A. Bernevig, "Hourglass fermions," Nature **532**, 189 (2016).

[55] B. J. Wieder, B. Bradlyn, Z. Wang, J. Cano, Y. Kim, H.-S. D. Kim, A. M. Rappe, C. L. Kane, and B. A. Bernevig, "Wallpaper fermions and the nonsymmorphic Dirac insulator," Science **361**, 246 (2018).

# Supplemental Materials on "Semi-Dirac and Weyl Fermions in Transition Metal Oxides"

Narayan Mohanta[1], Jong Mok Ok[1], Jie Zhang[1], Hu Miao[1], Elbio Dagotto[1,2], Ho Nyung Lee[1], Satoshi Okamoto[1]
[1]*Materials Science and Technology Division, Oak Ridge National Laboratory, Oak Ridge, TN 37831, USA*
[2]*Department of Physics and Astronomy, The University of Tennessee, Knoxville, TN 37996, USA*

## I. Details of *ab initio* calculations

The electronic structure was computed within *ab initio* density functional theory (DFT) [R2] as implemented in the QUANTUM ESPRESSO code [R3] with the plane-wave pseudopotential method. We adopted the Perdew-Burke-Ernzerhof generalized gradient approximation exchange-correlation functional [R4] and used a $16\times16\times16$ Monkhorst-Pack momentum-point mesh to discretize the first Brillouin zone. A plane wave cut-off of 600 eV, which were found to be sufficient to achieve convergence of the total energy. The energy convergence criterion was set to $10^{-6}$ eV during the minimization process of the self-consistent cycle. Starting with the experimental lattice constants $a=5.518$ Å, $b=5.518$ Å, and $c=8.280$ Å [R5], full optimization of the crystal structure was performed using the force convergence criterion of $10^{-3}$ eV/Å.

The Bloch wave functions, obtained from the DFT calculations, were used to construct the maximally localized Wannier functions [R6–R9]. Starting from an initial projection of atomic d-basis functions belonging to the $t_{2g}$ manifold and centered on metal sites, the $t_{2g}$-like Wannier functions were obtained. Using the tight-binding Hamiltonian, formulated using the $t_{2g}$ orbitals and obtained from Wannier90, the topological invariant was computed within the Wannier charge center formalism using the WannierTools code [R10, R11].

## II. Tight-binding model

To gain insight into the nature of the semi-Dirac dispersions in $t_{2g}$ perovskite transition-metal oxides with the $I4/mcm$ crystalline symmetry, we develop an effective tight-binding Hamiltonian.

For the sake of simplicity, we define the local orbitals as $\{a,b,c\}=\{d_{xy},d_{yz},d_{zx}\}$, and denote the hopping integral from orbital $\beta$ to $\alpha$ along the $h\hat{x}+k\hat{y}+l\hat{z}$ direction as $t^{\alpha\beta}_{hkl}$. This leads to the following tight-binding Hamiltonian:

$$H_{\rm TB}=-\sum_{\alpha,\beta}\sum_{\vec{r},\vec{r}'}\sum_{\sigma}t^{\alpha\beta}_{\vec{r}-\vec{r}'}\alpha^{\dagger}_{\vec{r}\sigma}\beta_{\vec{r}'\sigma}, \tag{E1}$$

where $\alpha^{(\dagger)}_{\vec{r}\sigma}$ is an annihilation (creation) operator of an electron on orbital $\alpha$ at position $\vec{r}$ with spin $\sigma$. Typical hopping integrals are presented in Fig. S1. The amplitude and the sign of $t^{\alpha\beta}_{hkl}$ are determined by the relative direction and the sign of two orbitals and must satisfy the underlying $I4/mcm$ symmetry. This leads to the following relations:

$$\begin{gathered}
t^{aa}_{100}=t^{aa}_{\bar{1}00}=t^{bb}_{010}=t^{bb}_{0\bar{1}0},\\
t^{aa}_{010}=t^{aa}_{0\bar{1}0}=t^{bb}_{100}=t^{bb}_{\bar{1}00},\\
t^{aa}_{001}=t^{aa}_{00\bar{1}}=t^{bb}_{001}=t^{bb}_{00\bar{1}},\\
t^{a'b}_{100}=t^{a'b}_{\bar{1}00}=t^{a'b}_{010}=t^{a'b}_{0\bar{1}0}=-t(\{a,b\}\leftrightarrow\{a',b'\}),\\
t^{ab}_{001}=t^{ab}_{00\bar{1}},\\
t^{cc}_{100}=t^{cc}_{\bar{1}00}=t^{cc}_{010}=t^{cc}_{0\bar{1}0},\\
t^{cc}_{001}=t^{cc}_{00\bar{1}}
\end{gathered} \tag{E2}$$

for the nearest-neighbor bonds, and

$$\begin{gathered}
t^{aa}_{110}=t^{aa}_{\bar{1}\bar{1}0}=t^{bb}_{\bar{1}10}=t^{bb}_{1\bar{1}0}=t^{b'b'}_{110}=t^{b'b'}_{\bar{1}\bar{1}0}=t^{a'a'}_{\bar{1}10}=t^{a'a'}_{1\bar{1}0},\\
t^{aa}_{1\bar{1}0}=t^{aa}_{\bar{1}10}=t^{bb}_{110}=t^{bb}_{\bar{1}\bar{1}0}=t^{b'b'}_{1\bar{1}0}=t^{b'b'}_{110}=t^{a'a'}_{110}=t^{a'a'}_{\bar{1}\bar{1}0},\\
t^{ab}_{110}=t^{ab}_{\bar{1}\bar{1}0}=-t^{ab}_{1\bar{1}0}=-t^{ab}_{\bar{1}10},\\
t^{cc}_{1\bar{1}0}=t^{cc}_{\bar{1}10}=t^{cc}_{\bar{1}10}=t^{cc}_{1\bar{1}0},\\
t^{aa}_{011}=t^{aa}_{0\bar{1}\bar{1}}=t^{aa}_{0\bar{1}1}=t^{aa}_{01\bar{1}}=t^{bb}_{101}=t^{bb}_{\bar{1}0\bar{1}}=t^{bb}_{\bar{1}01}=t^{bb}_{10\bar{1}},\\
t^{aa}_{101}=t^{aa}_{\bar{1}0\bar{1}}=t^{aa}_{\bar{1}01}=t^{aa}_{1\bar{0}1}=t^{bb}_{011}=t^{bb}_{0\bar{1}\bar{1}}=t^{bb}_{0\bar{1}1}=t^{bb}_{01\bar{1}},\\
t^{ac}_{101}=t^{ac}_{\bar{1}0\bar{1}}=-t^{ac}_{\bar{1}01}=-t^{ac}_{1\bar{0}1}=t^{bc}_{011}=t^{bc}_{0\bar{1}\bar{1}}=-t^{bc}_{0\bar{1}1}=-t^{bc}_{01\bar{1}},\\
t^{bc}_{101}=t^{bc}_{\bar{1}0\bar{1}}=t^{ac}_{011}=t^{ac}_{0\bar{1}\bar{1}}=-t^{bc}_{10\bar{1}}=-t^{bc}_{01}=-t^{ac}_{01\bar{1}}=-t^{ac}_{0\bar{1}1}=-t(\{a,b,c\}\leftrightarrow\{a',b',c'\})
\end{gathered} \tag{E3}$$

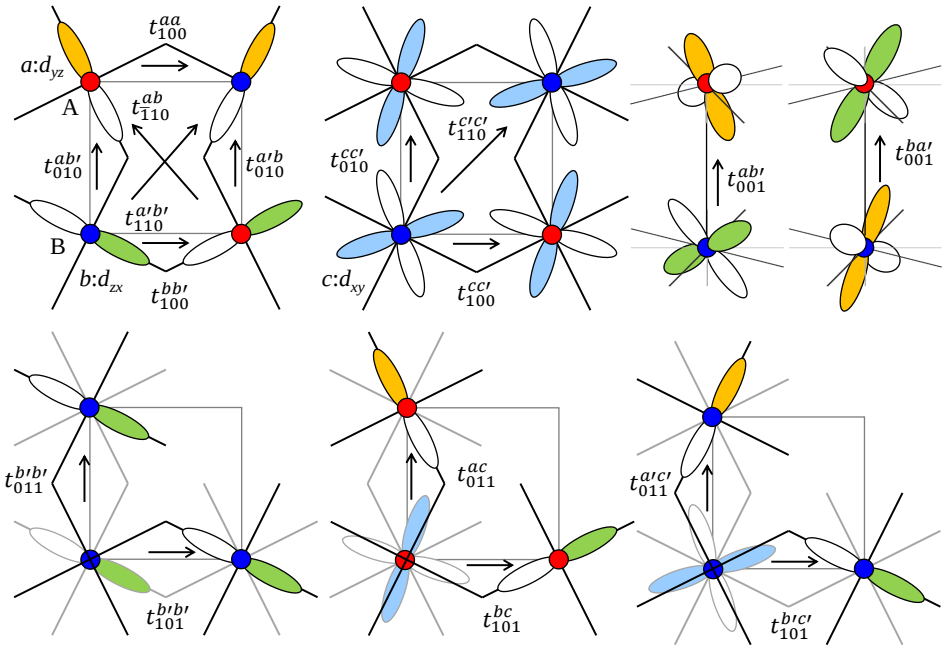


FIG. S1. Typical hopping integrals. Hopping integral from orbital $\beta$ to orbital $\alpha$ along the $h\hat{x}+k\hat{y}+l\hat{z}$ direction $t^{\alpha\beta}_{hkl}$ is indicated by an arrow. Here, red and blue circles belong to sublattice A and B, respectively. Orbitals $a: d_{yz}$, $b: d_{zx}$, and $c: d_{xy}$ are indicated by orange, green, blue robes, respectively. To highlight the sign difference in electron orbitals, negative regions are shown in white. Solid lines indicate how $O_6$ octahedra rotate, creating bond angles smaller than 180 degrees. In the second row, hopping is between second-neighbor sites on two adjacent layers.

for the second-neighbor bonds, and the elements that are not listed here are zero up to second-neighbor bonds. When the hopping integral depends explicitly on the sublattice A and B, we use $\{a', b', c'\}$ for sublattice B. Further-neighbor hopping integrals could be considered, but including these terms does not alter our discussion.

In the undistorted perovskite structure, many hopping integrals disappear reflecting the symmetry (positive and negative sign of $t_{2g}$ orbitals). Among such hopping integrals, non-zero value of $t^{ac}_{101}$ and symmetry related hopping as well as finite spin-orbit coupling are found to lift the band degeneracy of nodal lines along the P-N direction, creating semi-Dirac dispersions at the P point and Dirac dispersions at the N point.

In addition to the hopping integrals, there could exist crystal field splitting between orbitals $a$, $b$, and $c$ as

$$H_{\rm CFS} = \sum_{\sigma} \left\{ \varepsilon_{ab}(a^{\dagger}_{\sigma}a_{\sigma} + b^{\dagger}_{\sigma}b_{\sigma}) + \varepsilon_{c}c^{\dagger}_{\sigma}c_{\sigma} \right\}, \tag{E4}$$

where $a$ and $b$ remain degenerate in the $I4/mcm$ symmetry.

Finally, as the most important ingredient, the spin-orbit coupling is included. Here, we consider the atomic-like form given by

$$H_{\rm SOC} = \lambda \left(\vec{l}\cdot\vec{s}\right)_{t_{2g}} = \frac{\lambda}{2} \sum_{\alpha,\beta,\gamma} \sum_{\sigma,\sigma'} i\varepsilon_{\alpha\beta\gamma}\alpha^{\dagger}_{\sigma}\sigma^{\gamma}_{\sigma\sigma'}\beta_{\sigma'}, \tag{E5}$$

where $(\ldots)_{t_{2g}}$ indicates the projection onto the $t_{2g}$ subspace, $\alpha$, $\beta$, and $\gamma$ are orbital indices, $\sigma^{\gamma}$ is the Pauli matrix, and $\varepsilon_{\alpha\beta\gamma}$ is the Levi-Civita antisymmetric tensor. For $H_{\rm CFS}$ and $H_{SOC}$, site indices are omitted for simplicity.

Thus, the effective Hamiltonian is given by the sum of the above three terms:

$$H_{\rm eff} = H_{\rm TB} + H_{\rm CFS} + H_{\rm SOC}. \tag{E6}$$

In an example we show here, the following parameter set is considered: $t^{aa}_{100} = t^{aa}_{001} = t^{cc}_{100} = t$, $t^{aa}_{010} = t^{cc}_{001} = 0.1t$, $t^{a'b}_{100} = 0.05t$, $t^{a'b}_{001} = 0.1t$, $t^{cc}_{110} = t^{aa}_{011} = 0.4t$, $t^{aa}_{1\bar{1}0} = 0.1t$, $t^{ab}_{110} = 0.1t$, $t^{ac}_{101} = 0.05t$, $\varepsilon_c = 0.2t$, $\lambda = 0.5t$, and others are set to zero. Resulting dispersion relation is summarized in Fig. S2. One notices that this tight-binding dispersion

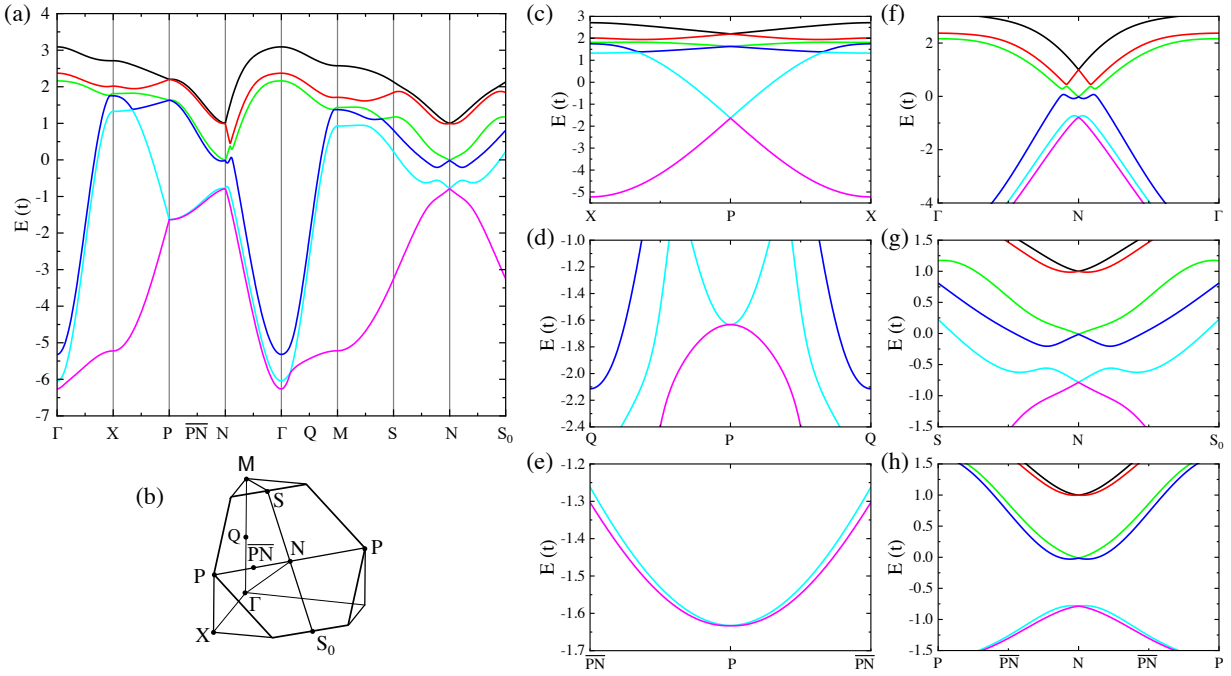


FIG. S2. Tight-binding dispersions. (a) Dispersions in the entire Brillouin zone with its first octant shown in (b). Dispersions around the P point and the N point are shown in panels (c-e) and (f-h), respectively. The midpoint between P and N is labeled as $\overline{\text{PN}}$.

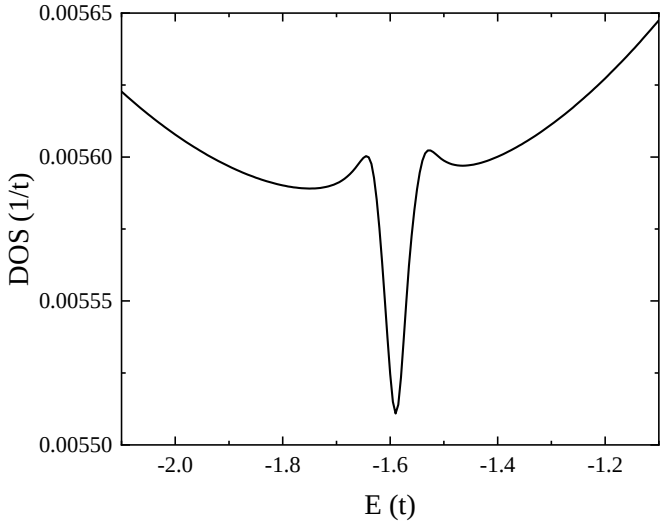


FIG. S3. Partial density of states originating from one of the semi-Dirac dispersions at the P point.

relation qualitatively reproduces the DFT dispersions, in particular semi-Dirac dispersions at the P point and the linear Dirac dispersion at the N point.

To see the consequence of the semi-Dirac dispersions, we computed the partial density of states (DOS) by focusing on one of the P points. The resulting DOS is shown in Fig. S3. Here, the momentum $\vec{k}$ integral is carried out in a small cube around the P point with $\Delta k = \pm\pi/8$ and the Dirac delta function approximated as the Lorentzian with the width $\eta = 0.02t$. One notices a sharp dip in DOS, instead of a gap, reflecting the semi-Dirac dispersions. With correlation effects, this may lead to novel many-body effects as discussed in Ref. [R1].

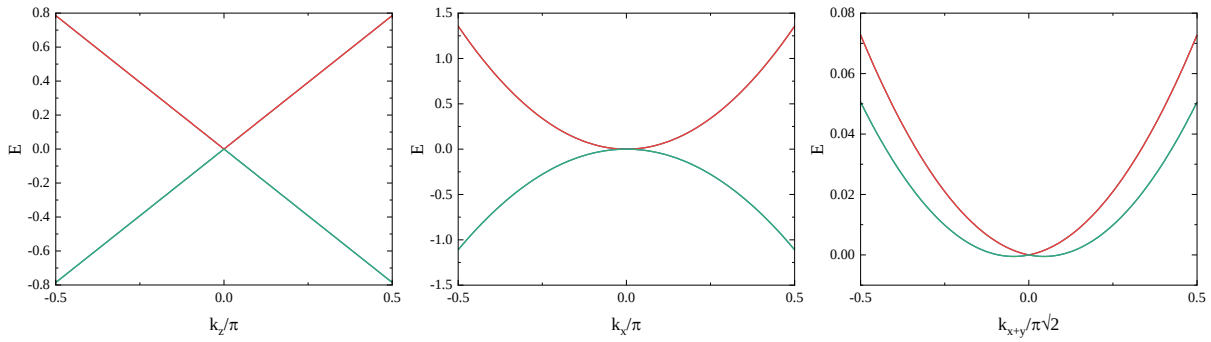


FIG. S4. Dispersion relation from the low-energy effective model Eq. (E9) along three inequivalent directions. Parameter values are chosen to be $A = -0.05$, $B = 0.01$, $C = 0.5$, and $D = 1.0$.

## III. Low-energy effective model

The tight-binding model developed in the previous section is useful to derive a low-energy effective model. For this purpose, we focus on the Kramers pairs that are eigenstates of local Hamiltonian, $H_{\rm CFS} + H_{\rm SOC}$. Such Kramers pairs may be expressed as

$$|\sigma = \pm 1\rangle \propto |a, \sigma\rangle + i|b, \sigma\rangle + \delta|c, -\sigma\rangle. \tag{E7}$$

Considering the hopping integrals described in the previous section, a low-energy Hamiltonian may be parameterized as

$$H_{\rm low\text{–}E} = -2A\cos k_x \cos k_y \tau_0\sigma_0 - B(\sin k_x \tau_3\sigma_1 - \sin k_y \tau_3\sigma_2)\sin k_z - \left\{2C(\cos k_x + \cos k_y) + D\cos k_z\right\}\tau_1\sigma_0, \tag{E8}$$

where $\tau_i$ and $\sigma_j$ are $2\times 2$ Pauli matrices acting on the sublattice space and the spin space specifying Kramers states, respectively, and Kronecker product are abbreviated as $\tau_i \otimes \sigma_j \equiv \tau_i\sigma_j$. Expanding cosine and sine functions at the P point $\vec{k} = (\pi, 0, \pi/2)$, and measuring the momentum from the P point, one arrives at

$$H_{\rm low\text{–}E} \approx -A\left(k_x^2 + k_y^2\right)\tau_0\sigma_0 - B(-k_x\tau_3\sigma_1 - k_y\tau_3\sigma_2) - \left\{C\left(k_x^2 - k_y^2\right) - Dk_z\right\}\tau_1\sigma_0, \tag{E9}$$

where a constant term is neglected from the diagonal component. The eigenvalues of this Hamiltonian are given by

$$E_\pm = A\left(k_x^2 + k_y^2\right) \pm \sqrt{B^2\left(k_x^2 + k_y^2\right) + \left\{C\left(k_x^2 - k_y^2\right) - Dk_z\right\}^2} \tag{E10}$$

In Fig. S4, we plot the dispersion relations along three different directions with $A = 0.05$, $B = 0.01$, $C = 0.5$, and $D = 1.0$. One can notice that this effective model gives essential feature of dispersions obtained in DFT and the tight-binding model; linear band crossing along the $k_z$ and the $k_x = \pm k_y$ directions, and quadratic band crossing along the $k_x$ and the $k_y$ directions. The band splitting along the $k_x = \pm k_y$ directions, corresponding to the P-N-P direction, is due to the parameter $B$, which corresponds to $t_{101}^{ac}$ and symmetry-related hopping terms.

## IV. Semi-Dirac points in the tetragonal oxides

The presence of the 3D semi-Dirac fermions was investigated in a few other compounds from the $I4/mcm$ space group, *viz*, $CaNbO_3$, $SrRuO_3$, $SrMoO_3$, and $SrTiO_3$. In Fig. S5, we show the electronic structures of these compounds that reveal the semi-Dirac points at the P point and Dirac points at the N point, similar to $SrNbO_3$. The semi-Dirac points in $CaNbO_3$ are located father away from the Fermi level than in $SrNbO_3$. In $SrRuO_3$, a semi-Dirac point at the P point is located very close to the Fermi level while the Dirac points at the N point are below the Fermi level. Furthermore, $SrRuO_3$ is known to have magnetic order which will split the semi-Dirac points to Weyl points, as described in the main text. In $SrMoO_3$, the semi-Dirac point at the P point is located even farther away from the Fermi level while three Dirac points at the N point are located very close to the Fermi level. With slight electron doping, these semi-Dirac points can appear at the Fermi level and contribute to the transport properties. Therefore, $SrMoO_3$ is another candidate material that can be interesting to look at to investigate the signatures of the semi-Dirac points. On the other hand, $SrTiO_3$ has the semi-Dirac points $\sim$2 eV above the Fermi level and hence they will not influence the transport properties. $SrTiO_3$, is therefore, useful as a substrate compound to control the epitaxial strain in the metallic tetragonal oxides.

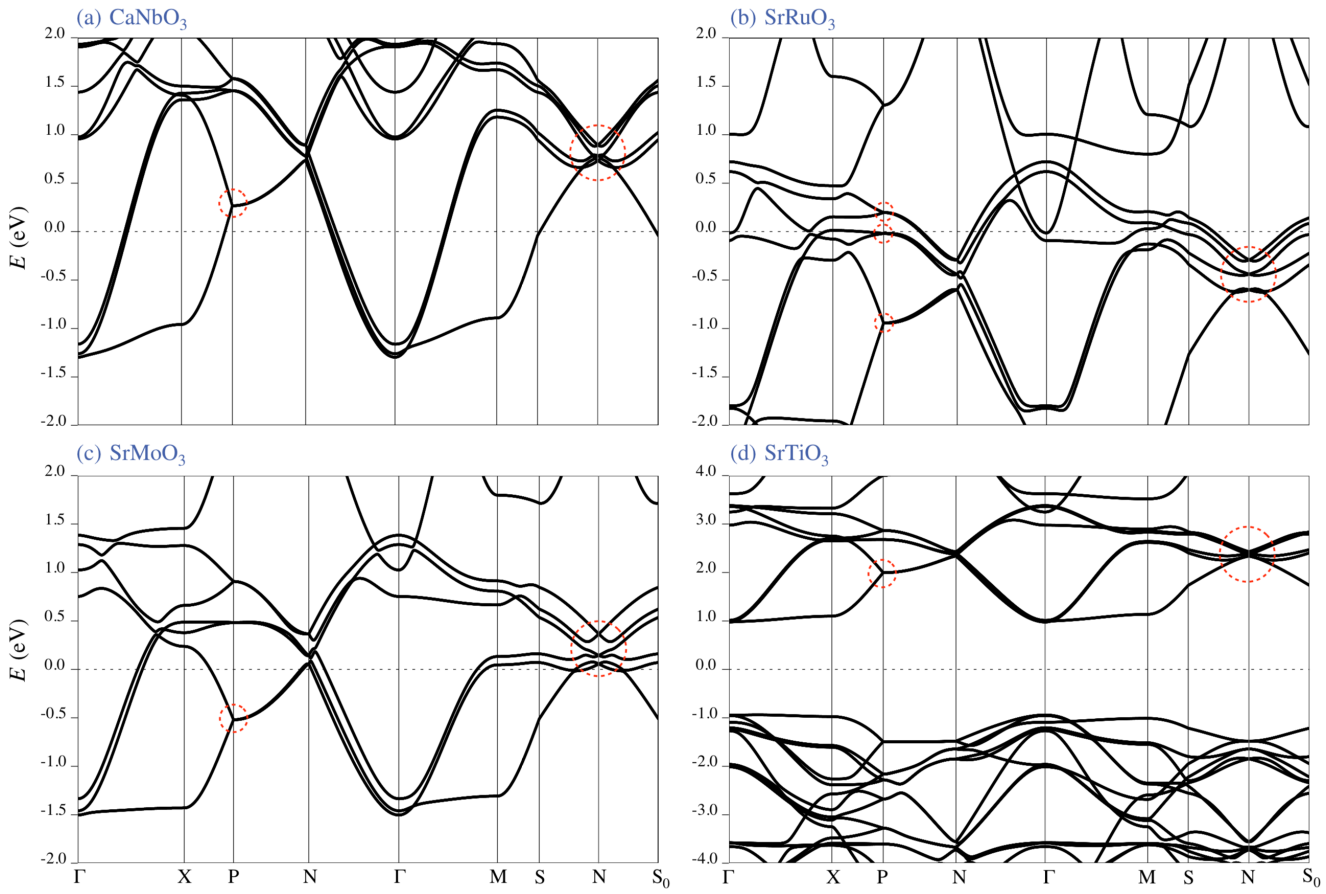


FIG. S5. DFT dispersions of tetragonal (a) $CaNbO_3$, (b) $SrRuO_3$, (c) $SrMoO_3$, and (d) $SrTiO_3$ in the presence of spin-orbit coupling. The red circles denote the three-dimensional semi-Dirac points at the P and the Dirac point at the N point. The lattice constants are: (a) $a = b = 5.560$ Å, $c = 8.018$ Å, (b) $a = b = 5.577$ Å, $c = 8.087$ Å, (c) $a = b = 5.621$ Å, $c = 8.078$ Å, (d) $a = b = 5.567$ Å, $c = 7.907$ Å.

## V. Octahedral rotation as a control parameter for the Berry curvature

The electronic properties of tetragonal $SrNbO_3$ were studied at several values of the rotation angle $\theta$ of $NbO_6$ octahedra. In experiments, $\theta$ can be tuned by controlling the epitaxial strain, via an effective interface engineering, changing the sample thickness, or an external electric field. In Fig. S6, the results at three values $\theta = 4°$, $\theta = 8°$ and $\theta = 16°$ are shown at a finite Nb spin polarization $M = 0.2$. The Berry curvature $\Omega$ exhibits peaks at the P point (center of the plane in (d)-(f)) and the N points (side corners of the plane) — the high-symmetry momenta at the Brilluoin zone boundary at which the semi-Dirac points appear. At the P point, $\Omega$ increases with increasing $\theta$ up to $\theta \approx 10°$, after which it decreases. On the other hand, $\Omega$ at the N points increases monotonically with increasing $\theta$ up to $\theta = 16°$. The energy separation between the two relevant bands near the semi-Dirac point, shown in Fig. S6(g)-(i) at the three values of $\theta$, also captures the substantial changes in the band dispersion. The change in the Berry curvature will consequently be noticeable in the intrinsic anomalous Hall conductivity $\sigma_{xy}$. The octahedral rotation, therefore, provides an additional control knob to tune the Berry phase properties in oxides.

## VI. Surface states in a slab (001) geometry

To study the nature of the surface states of tetragonal $SrNbO_3$, we calculate the band dispersion in a slab geometry. We consider a slab of thickness 40 unit cells oriented along the (001) direction, relevant to the common experimental situation, and use the tight-binding Hamiltonian, expressed in the basis of the Wannier orbitals. The band dispersion of the $SrNbO_3$ slab, along the high-symmetry momenta in the surface Brillouin zone, is shown in Fig. S7. In this case, the surface states do not exhibit any crossing-like feature, as expected. With a finite magnetization at the Nb site also, the surface states do not reveal any topological band crossing, as confirmed by the non-quantized anomalous

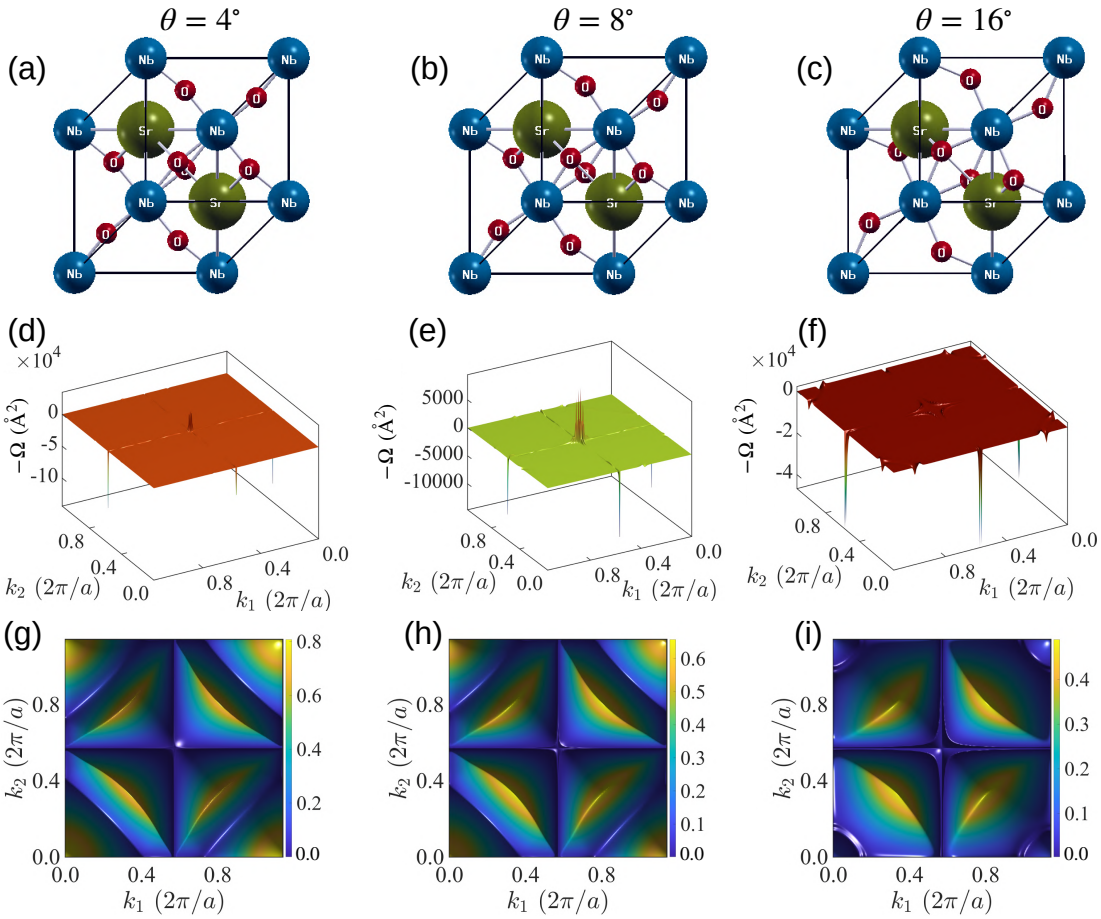


FIG. S6. Unit cell of tetragonal $SrNbO_3$ (top view) with different amount of the octahedral rotation: (a) $\theta = 4°$, (b) $\theta = 8°$, and (c) $\theta = 16°$. (d)-(f). Berry curvature at the respective values of $\theta$ with a Nb spin polarization $M = 0.2$. (g)-(i) Energy gap (in eV) between the two bands that connect the semi-Dirac point for the above three values of $\theta$. Evidently, with increasing the rotation angle $\theta$, there are drastic changes in the Berry curvature $\Omega$, and the energy gap between the Bloch bands near the semi-Dirac points.

Hall conductivity, as presented in the main text.


[R1] J.-R. Wang, W. Li, C.-J. Zhang, "Correlated interaction effects in three-dimensional semi-Dirac semimetal", arXiv:2101.05794.

[R2] P. Hohenberg and W. Kohn, "Inhomogeneous electron gas," Phys. Rev. **136**, B864 (1964).

[R3] P. Giannozzi, S. Baroni, N. Bonini, M. Calandra, R. Car, C. Cavazzoni, D. Ceresoli, G. L. Chiarotti, M. Cococcioni, I. Dabo, A. Dal Corso, S. de Gironcoli, S. Fabris, G. Fratesi, R. Gebauer, U. Gerstmann, C. Gougoussis, A. Kokalj, M. Lazzeri, L. Martin-Samos, N. Marzari, F. Mauri, R. Mazzarello, S. Paolini, A. Pasquarello, L. Paulatto, C. Sbraccia, S. Scandolo, G. Sclauzero, A. P. Seitsonen, A. Smogunov, P. Umari, and R. M. Wentzcovitch, "QUANTUM ESPRESSO: a modular and open-source software project for quantum simulations of materials," J. Phys. Condens. Matter **21**, 395502 (2009).

[R4] J. P. Perdew, K. Burke, and M. Ernzerhof, "Generalized gradient approximation made simple," Phys. Rev. Lett. **77**, 3865 (1996).

[R5] J. M. Ok, N. Mohanta, J. Zhang, S. Yoon, S. Okamoto, E. S. Choi, H. Zhou, M. Briggeman, P. Irvin, A. R. Lupini, Y.-Y. Pai, E. Skoropata, C. Sohn, H. Li, H. Miao, R. G. Moore, Z. Ward, B. J. Lawrie, W. S. Choi, G. Eres, J. Levy, and H. N. Lee, "Correlated oxide Dirac semimetal in the extreme quantum limit," Private communication.

[R6] N. Marzari and D. Vanderbilt, "Maximally localized generalized Wannier functions for composite energy bands," Phys. Rev. B **56**, 12847 (1997).

[R7] I. Souza, N. Marzari, and D. Vanderbilt, "Maximally localized Wannier functions for entangled energy bands," Phys. Rev. B **65**, 035109 (2001).

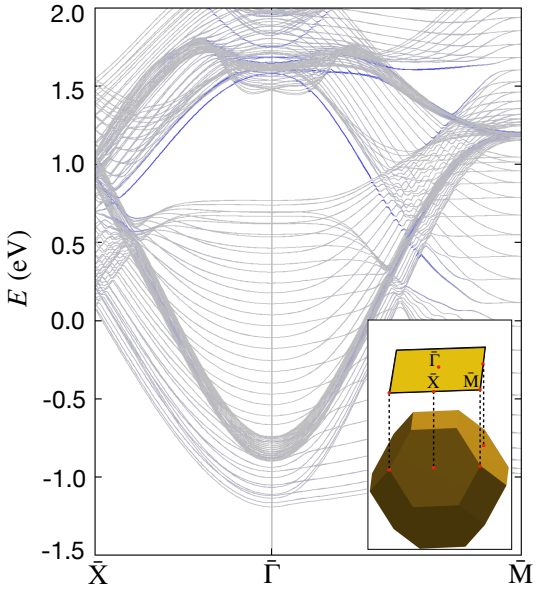


FIG. S7. Band dispersion of a (001) slab of tetragonal $SrNbO_3$, showing the surface states in blue and bulk states in grey along the high-symmetry momenta in the surface Brillouin zone, shown in the inset.


[R8] A. A. Mostofi, J. R. Yates, Y.-S. Lee, I. Souza, D. Vanderbilt, and N. Marzari, "Wannier90: A tool for obtaining maximally-localised Wannier functions," Comput. Phys. Commun. **178**, 685 (2008).

[R9] G. Pizzi, V. Vitale, R. Arita, S. Blügel, F. Freimuth, G. Géranton, M. Gibertini, D. Gresch, C. Johnson, T. Koretsune, J. Ibañez-Azpiroz, H. Lee, J.-M. Lihm, D. Marchand, A. Marrazzo, Y. Mokrousov, J. I. Mustafa, Y. Nohara, Y. Nomura, L. Paulatto, S. Poncé, T. Ponweiser, J. Qiao, F. Thöle, S. S. Tsirkin, M. Wierzbowska, N. Marzari, D. Vanderbilt, I. Souza, A. A Mostofi, and J. R. Yates, "Wannier90 as a community code: New features and applications," J. Phys. Condens. Matter **32**, 165902 (2020).

[R10] A. A. Soluyanov and D. Vanderbilt, "Computing topological invariants without inversion symmetry," Phys. Rev. B **83**, 235401 (2011).

[R11] Q. Wu, S. Zhang, H.-F. Song, M. Troyer, and A. A. Soluyanov, "WannierTools: An open-source software package for novel topological materials," Comput. Phys. Commun. **224**, 405 (2018).